UC Irvine
UC Irvine Previously Published Works

Title

Voltage-dependent structural models of the human Hv1 proton channel from long-timescale molecular dynamics simulations

Permalink

Journal

ISSN

Authors

Geragotelis, Andrew D
Wood, Mona L
Göddeke, Hendrik
et al.

Publication Date

DOI

Peer reviewed

Voltage-dependent structural models of the human Hv1 proton channel from long-timescale molecular dynamics simulations

Andrew D. Geragotelis[a], Mona L. Wood[a], Hendrik Göddeke[b], Liang Hong[c,1], Parker D. Webster[c,d], Eric K. Wong[a], J. Alfredo Freites[a], Francesco Tombola[c,d], and Douglas J. Tobias[a,2]

[a]Department of Chemistry, University of California, Irvine, CA 92697; [b]Theoretical Chemistry, Faculty of Chemistry and Biochemistry, Ruhr University Bochum, D-44780 Bochum, Germany; [c]Department of Physiology and Biophysics, University of California, Irvine, CA 92697; and [d]Chao Family Comprehensive Cancer Center, University of California, Irvine, CA 92697

The voltage-gated Hv1 proton channel is a ubiquitous membrane protein that has roles in a variety of cellular processes, including proton extrusion, pH regulation, production of reactive oxygen species, proliferation of cancer cells, and increased brain damage during ischemic stroke. A crystal structure of an Hv1 construct in a putative closed state has been reported, and structural models for the channel open state have been proposed, but a complete characterization of the Hv1 conformational dynamics under an applied membrane potential has been elusive. We report structural models of the Hv1 voltage-sensing domain (VSD), both in a hyperpolarized state and a depolarized state resulting from voltage-dependent conformational changes during a 10-μs-timescale atomistic molecular dynamics simulation in an explicit membrane environment. In response to a depolarizing membrane potential, the S4 helix undergoes an outward displacement, leading to changes in the VSD internal salt-bridge network, resulting in a reshaping of the permeation pathway and a significant increase in hydrogen bond connectivity throughout the channel. The total gating charge displacement associated with this transition is consistent with experimental estimates. Molecular docking calculations confirm the proposed mechanism for the inhibitory action of 2-guanidinobenzimidazole (2GBI) derived from electrophysiological measurements and mutagenesis. The depolarized structural model is also consistent with the formation of a metal bridge between residues located in the core of the VSD. Taken together, our results suggest that these structural models are representative of the closed and open states of the Hv1 channel.

Hv1 proton channel | open state model | closed state model | molecular dynamics simulations | ion channels

The voltage-gated proton channel (Hv1) is a proton-selective voltage-dependent channel whose primary function is to extrude acid from cells (1). Hv1 is expressed in many different types of cells, and it has been implicated in a wide range of biological processes, including intracellular pH regulation, the immune response, and sperm capacitation (2–8). Hv1 is also preferentially expressed in several types of cancers, such as B-cell malignancies (5, 9) and breast and colorectal cancers (10–12). Excessive Hv1 activity was found to increase the metastatic potential of cancer cells (9, 11). In the central nervous system, Hv1 is expressed in the microglia, where it is required for NADPH oxidase-dependent reactive oxygen species production. Microglial Hv1 activity was found to exacerbate brain damage after ischemic stroke (13) in an age-dependent manner (14). The numerous and diverse biological processes in which Hv1 is involved make the channel a promising pharmacological target. Hv1 inhibitors, for instance, could find applications as anticancer drugs or neuroprotective agents (15, 16).

Hv1 is a member of the superfamily of proteins containing voltage-sensing domains (VSDs), which are evolutionarily conserved functional modules that regulate the opening of voltage-dependent ion channels (17). But, in contrast to voltage-dependent metal-ion channels, Hv1 does not possess a separate pore domain (18, 19). The VSD in Hv1 comprises four transmembrane helical segments (S1 through S4), as well as an S0 helix at the N terminus and a coiled-coil region at the C terminus. The native functional unit of Hv1 is a homodimer, but removal of the C-terminal helix results in functional monomer units (20, 21). Thus, the Hv1 monomer contains both the proton current gate and the proton-conduction pathway.

As with other VSD-containing proteins, the voltage sensitivity of Hv1 is conferred by the S4 helix, which moves within the membrane in response to changes in the applied membrane potential (reviewed in ref. 17). The S4 helix contains three conserved triplet repeats, composed of an arginine followed by two hydrophobic residues. These arginine residue side chains interact with acidic side chains on the S1–S3 helices, forming an internal salt-bridge network. These salt-bridges are exchanged between the acidic residues on S1–S3 during the movement of S4 and subsequent activation of the channel (22–25).

Significance

The Hv1 voltage-gated proton channels are important for various physiological functions that include the extrusion of acid from cells, oxidative bursts in phagocytes, and immune response. A lack of structural information under physiological conditions has left many unanswered questions about the mechanism of proton conduction. We employed molecular dynamics simulations to generate structural models of the open and closed states of the channel in the presence of applied membrane potentials, without any initial assumptions on the position of the voltage sensor and without relying on homology on functional similarities between Hv1 and other voltage-sensitive proteins. We have thus provided molecular-scale insights into the mechanism of voltage-dependent activation that could inform therapeutic strategies for modulating the function of Hv1.

A crystallographic structure of a chimeric construct based on mouse Hv1 (mHv1cc) was solved to a 3.45-Å resolution by Takeshita et al. (26). This structure provides a putative model for the closed state of the channel. However, the reported structure is in a nonphysiological trimeric configuration and does not provide any direct information on the open state or the interface between Hv1 subunits. More recently, a solution NMR structure of the human Hv1 (hHv1) VSD in a micellar environment has been reported (27). This structure was proposed to represent an intermediate conformation between the resting and activated states. Several models of the Hv1 open state generated by using atomistic molecular dynamics (MD) simulations have been reported (28–32). However, these models were based on crystallographic structures of K^+ or Na^+ voltage-gated channels, in which there is not a native permeation pathway through the VSD (28–30, 32), or used artificial restraints to produce alternative VSD conformations (31). Here, we report structural models of the Hv1 VSD consistent with the open and closed states of the channel generated, exclusively, from the action of an applied membrane potential in atomistic MD simulations initiated from a homology model using the crystal structure of the monomer in the mouse chimeric construct as the template. We demonstrate that our structural models are consistent with a variety of experimental functional data in the literature, as well as experimental metal-bridging data reported herein.

Results

We constructed an all-atom model of the hHv1 channel VSD embedded in a lipid bilayer using the mHv1cc crystal structure (26) as a template for the protein chain (see *Materials and Methods* for details). The model consists of a monomeric hHv1 VSD (residues 88 to 230) in a 1-palmitoyl-2-oleoyl-*sn*-glycero-3-phosphocholine (POPC) bilayer in excess hydration. The Hv1 VSD conformational dynamics relevant to function occurs under an applied membrane potential. Thus, in order to characterize both the structure of the membrane-embedded hHv1 VSD and its voltage-dependent conformational changes, we generated an ~33-μs MD simulation trajectory, in which the simulation system was subjected to an applied membrane potential, generated by applying a uniform electric field along the transmembrane direction to all of the atoms in the system, with the schedule shown in Fig. 1*A*.

Equilibration of the membrane-embedded hHv1 VSD comparative model required several microseconds of simulation trajectory in the absence of a membrane potential (*SI Appendix*, Fig. S1). The accommodation of the protein in the membrane environment during the unpolarized portion of the simulation trajectory (~7.3 μs) led to an overall change in the configuration of the VSD helix bundle relative to the mHv1cc crystal structure. This process resulted in the formation of a salt-bridge network in the VSD intracellular half between the three basic arginine residues on the S4 helix and acidic residues on the S1–S3 helices that was distinct from the one observed in the crystallographic structure (*SI Appendix*, Fig. S2). In particular, sustained salt-bridge configurations were formed between R205 and D112 and between R211 and D174, while R208 switched salt-bridge partners from D112 (observed in the crystallographic structure) to D185 within the first microsecond of simulation trajectory (*SI Appendix*, Figs. S3 and S4). Upon membrane polarization to –150 mV relative to the intracellular side (after ~7.3 μs of simulation trajectory; Fig. 1*A*, *Top*), the S4 Arg side chains oriented toward the intracellular side (the direction of the membrane electric field), resulting in a rearrangement of the internal salt-bridge network from the unpolarized configuration below the R205–D112 salt-bridge, which remained unaffected by polarization (Fig. 1*B* and *SI Appendix*, Figs. S3 and S4). This change in the salt-bridge network was recorded as an effective charge displacement within the membrane electric field toward the

intracellular side (Fig. 1 *A*, *Middle*) without significant displacements of any of the helices (Fig. 1 *A*, *Bottom*).

Depolarization of the membrane to +150 mV (relative to the intracellular side) after ~11 μs of simulation trajectory elicited an effective charge displacement within the membrane electric field in two separate steps (Fig. 1 *A*, *Middle*). The first event occurred after the S4 arginine side chains promptly reoriented toward the extracellular side after the depolarization without any significant movement of the transmembrane helices (Fig. 1 *A*, *Bottom* and *SI Appendix*, Figs. S3 and S4). The change in the R205 conformation left the side chain above the level of F150, while still interacting with D112. R208 and R211 remained on the intracellular side, but with different solvation partners; R208 switched a salt-bridge from E153 to D112, and R211 formed a salt-bridge interaction with D174. The second charge displacement event, after ~22 μs of simulation trajectory, involved an upward movement of the S4 helix of ~8 Å along the transmembrane direction (Fig. 1 *A*, *Bottom* and *SI Appendix*, Fig. S5). Both R205 and R208 rapidly jumped toward the extracellular side, and R205 ended up at the polar/apolar membrane interface, where it also interacted with D123, while R208 remained in the extracellular vestibule, forming a salt-bridge configuration with E192 and E119 as partners. R211 remained at the level of F150, forming a salt-bridge with D112 (*SI Appendix*, Fig. S4 and Fig. S5).

The fully depolarized configuration (Fig. 1*C*) remained stationary under the depolarizing potential for an additional 12 μs. The final solvation partners of R211 include D112 and D185, while R208 and R205, having reached the extracellular surface of the protein, interact with E192/E119 and D123, respectively (*SI Appendix*, Figs. S3 and S4). The overall structural effect of the conformational changes between the hyperpolarized and fully depolarized configurations was a complete translocation of the internal salt-bridge interaction network from the intracellular half of the VSD permeation pathway to the extracellular side. (Fig. 1 *B* and *C* and *SI Appendix*, Fig. S3). The total gating charge displacement within the membrane electric field, ~2.7e (Fig. 1 *A*, *Middle* and *SI Appendix*, Fig. S6), was in line with the available experimental estimates (33–35).

The voltage-dependent internal salt-bridge rearrangement reshaped the VSD permeation pathway and the local water distribution in the region around F150 and D112 (Fig. 2*A* and *SI Appendix*, Fig. S7), but the water occupancy throughout the permeation pathway remained relatively stationary (Fig. 2*B*). Notably, the evolution of the frequency of fully connected H bond chains involving internal waters and acidic side chains (Fig. 2*C*) followed closely the evolution of the charge displacement within the membrane electric field (Fig. 1*C*). In particular, only the fully depolarized configuration exhibited a steady, nonzero, frequency of fully connected H bond chains. These results suggest that only the fully depolarized configuration would be suitable to carry out proton permeation from the intracellular side to the extracellular side through an H bond network formed by water molecules and acidic side chains. We posit, therefore, that the hyperpolarized and fully depolarized configurations of the hHv1 (Fig. 1 *D* and *E*) may describe, respectively, the closed and open states of the channel.

2-Guanidinobenzimidazole Binding. The ligand 2-guanidinobenzimidazole (2GBI) has been shown to block the open state of Hv1 from the intracellular side (36). Electrophysiological and mutagenesis data suggest a binding site formed by D112, F150, S181 (in S3), and R211, with the ligand's imidazole moiety forming polar interactions with D112 and R211/S181, the condensed phenyl ring near the F150 side chain, and the basic guanidine group near D112 (37). As a key step toward the validation of our fully depolarized configuration as an open state of the channel, we performed docking simulations of the
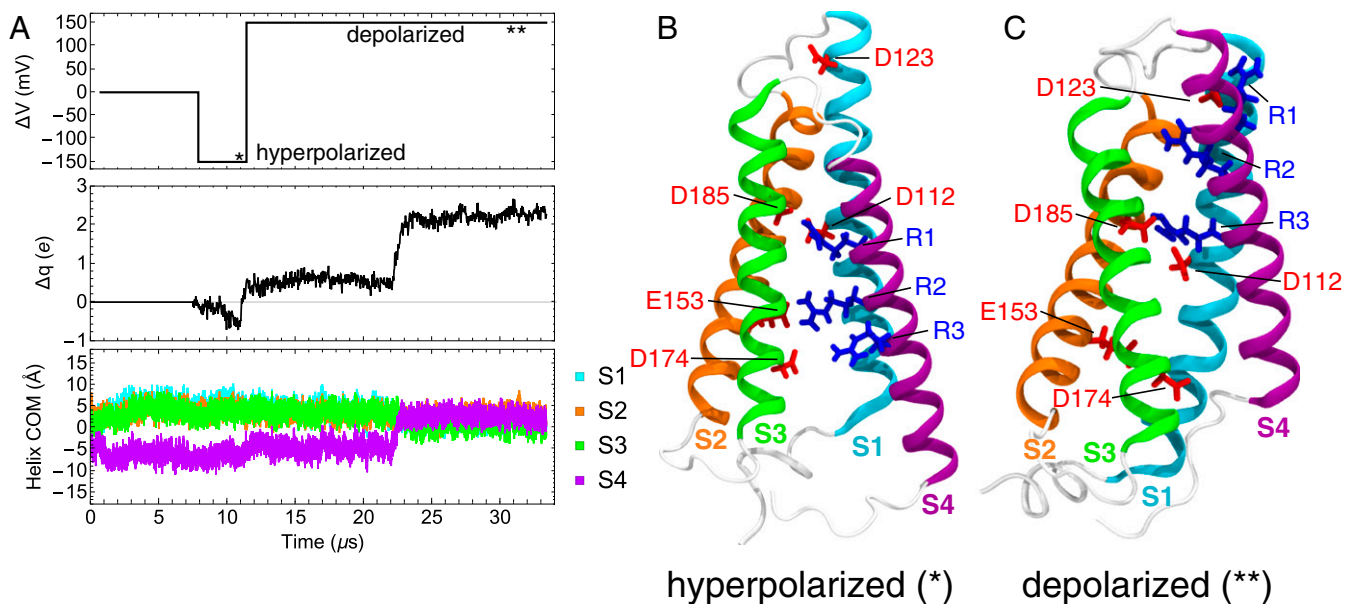
Fig. 1. MD simulations of the hHv1 in a hydrated lipid bilayer. (*A, Top*) Applied membrane potential protocol during a 33-μs simulation (the potential values are relative to the intracellular side of the membrane). (*A, Middle*) Total charge displacement in the membrane electric field. Switching the membrane potential from a hyperpolarizing potential to a depolarizing potential after ~11 μs of simulation trajectory results in a net charge displacement of ~2.72 ± 0.04 in two separate shot-like events of ~0.9e (shortly after the potential switch) and ~1.8e (at 22 μs). (*A, Bottom*) Centers-of-mass (COM) trajectories of the S1 to S4 helices. The helices COM positions remain essentially stationary up to the second gating charge displacement event, which involves an ~8-Å upward displacement of the S4 helix along the transmembrane direction. (*B* and *C*) The overall net charge displacement involves a full translocation of the internal salt-bridge interaction network from the intracellular half of the VSD permeation pathway to the extracellular side, as illustrated by the VSD snapshots of the hyperpolarized configuration at 11 μs (*) (*B*); and the fully depolarized configuration at 30 μs (**) (*C*). Conserved basic side chains in S4 (labeled R1 to R3, corresponding to residues R205, R208, and R211) and acidic side chains in S1 to S3 are shown in licorice representation (blue and red, respectively).

2GBI ligand probing the suggested binding site (Fig. 3). The search space for the docking simulations included the entire intracellular vestibule up to the R211–D112 pair, so as not to bias the selection of the binding-site prediction (using a total search space volume of 33 × 33 × 24 Å; *SI Appendix*, Fig. S8).

The fully depolarized model showed favorable binding of 2GBI with the aromatic group next to F150 and the guanidine group pointed between D112 and R211 (Fig. 3 *A* and *B*). The ligand was positioned directly below the R211–D112 pair, effectively blocking the formation of a fully connected H bond configuration throughout the VSD permeation pathway (Fig. 3*C*). This ligand-bound configuration remained stationary, and the ligand did not unbind during a 55-ns simulation trajectory (Fig. 3 *D* and *E*). A similar docking calculation on the hyperpolarized configuration revealed that the orientation of the selected residues does not allow the 2GBI to find a favorable binding conformation (*SI Appendix*, Fig. S8).

Internal Cross-Link Inhibits Conduction. The use of cross-links between residues on neighboring subunits can provide information about residue side chain proximity. This can be achieved by using engineered cysteine cross-links through a metal-ion bridge, which allows for the protein to maintain its physiological conformation (38–41). Residue V109 in S1 has been experimentally shown to face the VSD permeation pathway (42, 43), and in an earlier up-state model of hHv1 (28), it was predicted to be in the vicinity of F150. We expressed in *Xenopus* oocytes a monomeric version of Hv1 (21, 44) (see *Materials and Methods* for details), in which the only endogenous cysteine in the VSD, C107, was replaced by an alanine (background) or versions of the same channel containing one single amino-acid substitution, V109C or F150C, or the double substitution V109C/F150C. From these oocytes, we measured proton currents elicited by membrane depolarization in inside-out patch configuration, in the absence

of Cd^{2+} and in the presence of 2 μM Cd^{2+} in the intracellular solution (Fig. 4*A*). The current carried by the V109C/F150C double mutant was reduced by 80 to 90% in the presence of Cd^{2+}, while the currents carried by the channels with the single substitutions and the background Hv1 were only reduced by ~10% (Fig. 4*B*). After addition of Cd^{2+}, the current carried by the V109C/F150C displayed a biphasic behavior (Fig. 4 *A*, *Inset*). Upon membrane depolarization, the current transiently increased to a maximal level and then decreased to a steady-state level, producing a peak that is a hallmark of open-channel block. The results indicated that Cd^{2+} must wait for the Hv1 VSD to open in order to affect the current and that, in the open state, the cysteines at positions 109 and 150 are close enough to coordinate the cadmium ion and stabilize its binding to the channel, consistent with the formation of a Cd bridge.

We performed a 70-ns MD simulation of the F150C–V109C mutant in the fully depolarized configuration, including a harmonic restraint between the Cys beta carbons to model the metal bridge. We found that the artificial cross-link could be sustained, exclusively, with a rearrangement of the mutated side chains without large protein backbone movements (Fig. 4*C*). An additional 75-ns simulation with the restraint removed produced only a minor conformational drift (*SI Appendix*, Fig. S9).

Discussion

The mechanism of voltage sensing is expected to be similar in Hv1 and other voltage-gated ion channels. In particular, the availability of evolutionarily conserved salt-bridge partners in the core of the VSD allows the S4 arginines to remain fully solvated within the membrane electric field, thereby allowing the translocation of the S4 helix upon changes in membrane potential. However, in contrast to the VSDs of other channels, the S4 arginines in Hv1 must share internal crevices with the proton-conduction pathway, resulting in a direct coupling between the
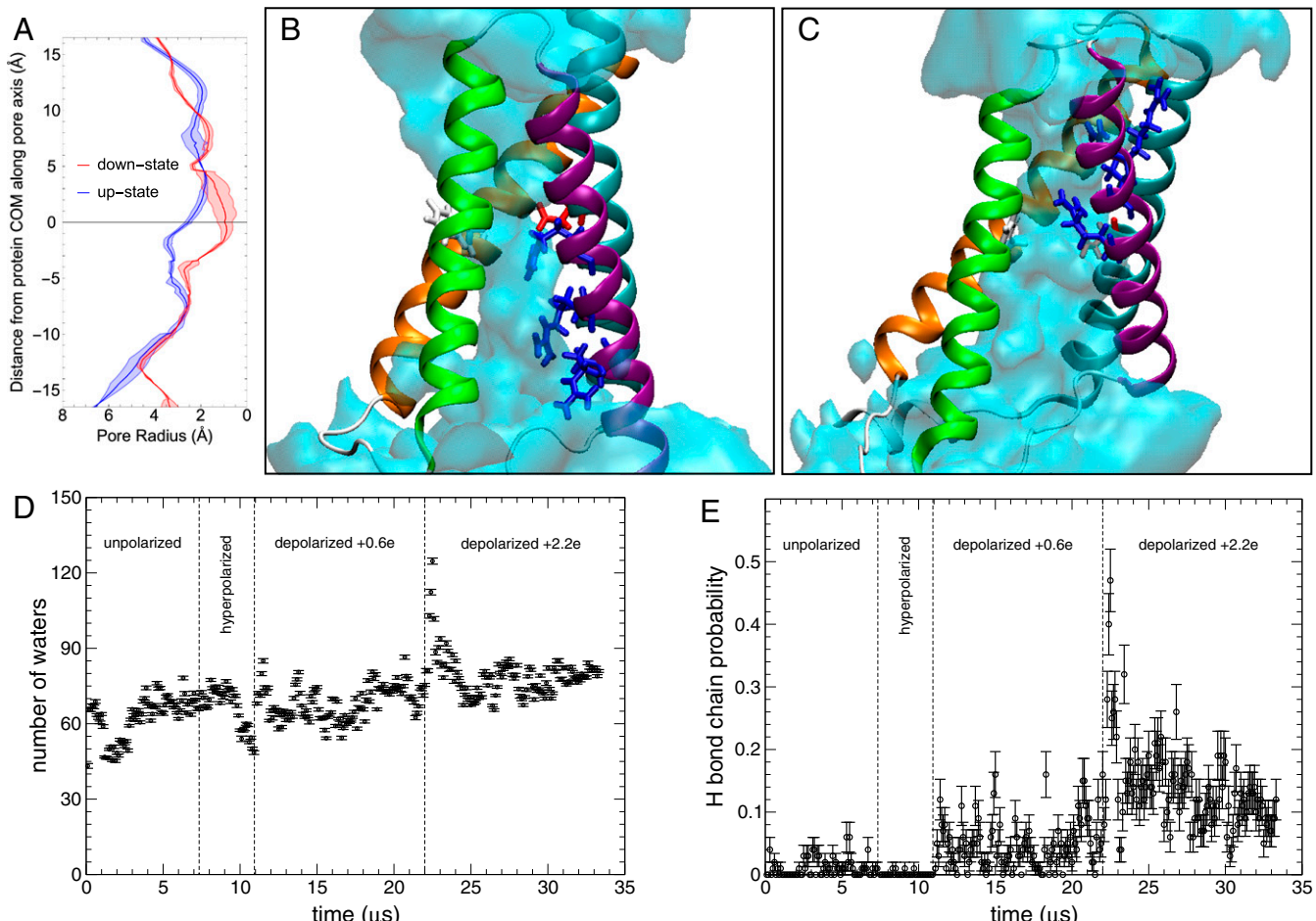
Fig. 2. Structural and dynamical features of the Hv1 VSD permeation. (*A*) Permeation pathway radius profile for the hyperpolarized state (red) and fully depolarized state (blue). (*B* and *C*) Protein configuration snapshots for the hyperpolarized state (*B*) and fully depolarized state (*C*) with the corresponding bulk water isodensity surface. The permeation pathway has a central constriction at the level of F150/D112. (*D*) Except for a few transient features attributable to the instantaneous changes of membrane potential, the number of waters within the VSD permeation pathway remains essentially stationary along the simulation trajectory. (*E*) The frequency of fully connected H bond chains formed between waters and acidic side chains throughout the VSD permeation pathway correlates well with the membrane-potential schedule. Sustained connected H bond chains are only observed in the fully depolarized conformation. COM, center of mass.

motion of the arginines and channel gating. The atomistic simulations of the hHv1 VSD in a membrane environment under an applied potential reported here offer testable models for both the open and closed states of the channel and the structural features involved in the voltage-dependent activation. We have shown that both the closed-to-open transition observed in our simulations and the resulting configuration under a depolarizing potential are consistent with the available experimental evidence.

Over the microsecond timescale, several key changes arise from the starting configuration based on the Hv1–CiVSP chimera crystallographic structure. During the unpolarized portion of the simulation, the S3 helix shifts toward the extracellular side by approximately one helical turn compared to the crystallographic structure, suggesting that S3 sits higher in the membrane. A similar observation was made by using electron paramagnetic resonance (EPR) measurements on hHv1 at 0 mV (45). This shift puts V178 in better alignment with F150 to form a hydrophobic gasket, a finding consistent with a recent study that probed the gasket stability in the closed state (43). The S4 helix gating charges are straddling this position with the lower two arginine residues, R208 and R211, sitting closer to the intracellular side of the pore, with R205 just above F150. This facilitates

interactions between D112 and R205 in the unpolarized configuration, with the R208–E153 and R211–D174 salt-bridges both below the hydrophobic gasket defined by F150 and V178. The second upper hydrophobic gasket seen in the crystal structure does not appear in our unpolarized configuration, leading to just a single solvent constriction site with low water density.

In a large deviation from the crystal structure, the S2 helix tilts to the side, creating a wider intracellular gap between S1 and S2. Likewise, S4 tilts away from S3, widening the intracellular gap between these two helices. Because our structural model lacks a coiled-coil domain, we wondered whether these reorganizations of the VSD helix bundle could be due to the unraveling of the VSD C terminus. However, running an additional 1-μs simulation with the C terminus truncated at R223 did not result in any large protein backbone rearrangements (*SI Appendix*, Fig. S10). While this segment would normally be part of the coiled-coil motif responsible for dimerization extending out into the cytosol, it likely does not serve a functional purpose in the monomeric channel. We conclude that the widening of the pore we observed, with respect to the crystallographic structure, is most likely a consequence of Hv1 VSD solvation in the membrane environment.
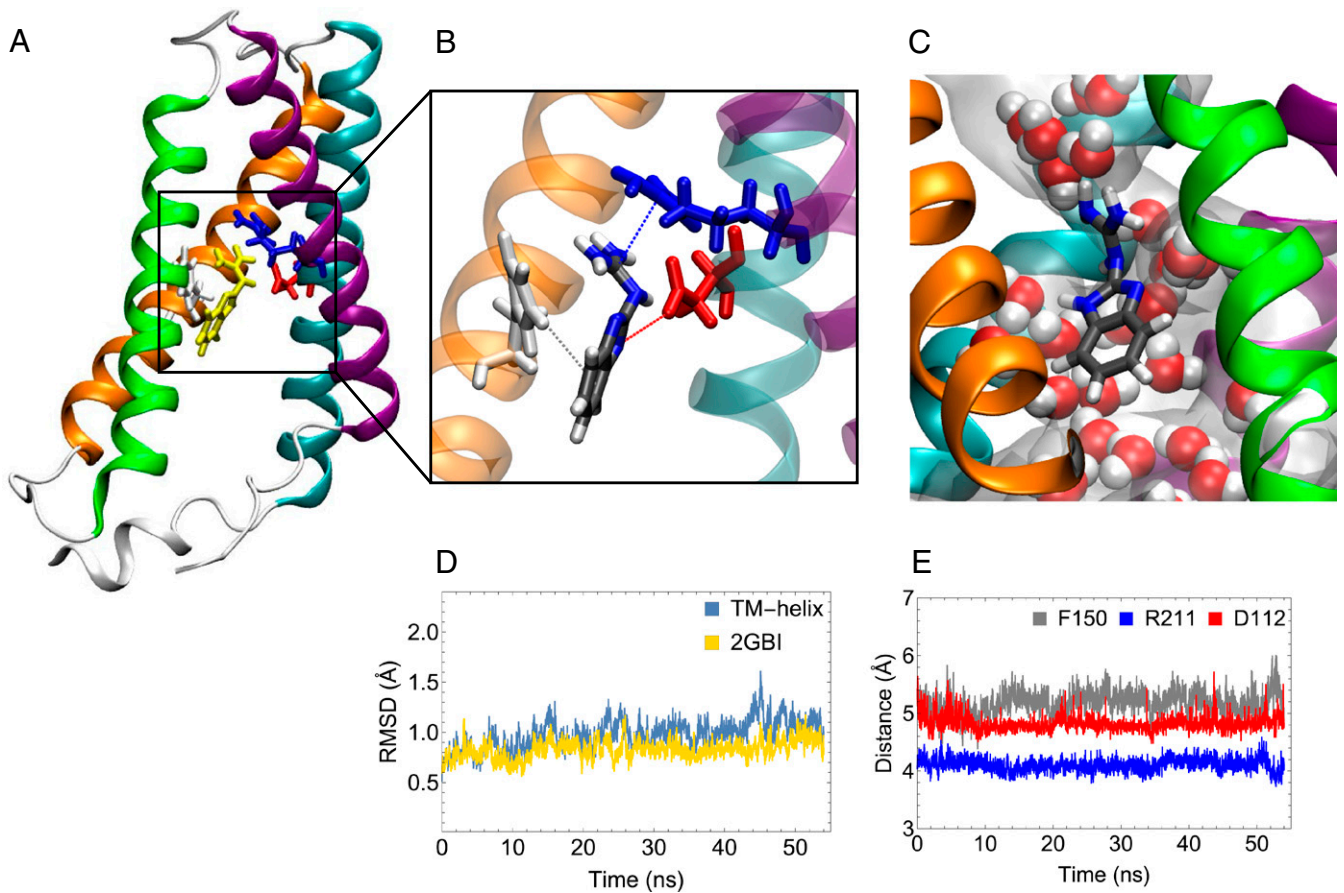
Fig. 3. Binding of the Hv1 inhibitor, 2GBI, and MD equilibration. (*A*) Configuration snapshot of the equilibrated binding mode. Shown are 2GBI (in yellow) and the interacting residues in licorice representation. (*B*) A zoom-in on the interactions between 2GBI (colored by atom) and R211 (blue), D112 (red), and F150 (white). (*C*) The 2GBI blocks the formation of a continuous water wire. (*D*) The rmsd from the initial configuration over a 54-ns trajectory of one of the selected docking poses for the VSD helix Cα atoms (blue) and the 2GBI heavy atoms (yellow). (*E*) The atomic distances between 2GBI and the selected residues measured as a function of the simulation time. The 2GBI–F150 distance is measured from the center of the benzyl rings; the 2GBI–R211 distance is measured from the carbon atoms of the guanidine groups; and the 2GBI–D112 distance is measured from the imidazole nitrogen on 2GBI to the nearest oxygen of the D112 carboxyl group. TM, transmembrane.

Comparisons with Other Models. Our fully depolarized configuration differs from previous up-state models of the Hv1 VSD generated by using the structures of VSDs from Kv and Nav channels as templates (28–30, 32). In our model, F150 sits at the center of the water-constriction site, and all three S4 arginine residues move above F150, with R211 in line with D112 and D185 in the fully depolarized configuration, as also suggested by Wood et al. (28). However, the positioning of the evolutionarily conserved acidic residues is different from those in both homology models proposed by Wood et al., R1-Hv1 and R2-Hv1. The first arginine of Hv1 is aligned with the first gating charge position in the Kv1.2–2.1 paddle-chimera structure in R1-Hv1 and with the second gating charge position in R2-Hv1. In both models, D185 is positioned higher in the extracellular vestibule, while D112 sits on the inner side of the constriction region, just above the intracellular vestibule (28). R211 is located between the two negatively charged residues in R1-Hv1 and below D112 in R2-Hv1, which prevents direct R211–D185 interactions in both cases. Likewise, in the R3D hHv1 homology model developed by Kulleperuma et al. (29), using the VSDs from KvAP, the Kv1.2–2.1 paddle chimera, and NavAb as templates, R211 is in line with D112 located near the center of the pore. In their model, D185 on the S3 helix also sits well within the extracellular vestibule quite far from the D112–R211 salt-bridge. Repositioning of the S3 helix in these models in the manner suggested by EPR experiments (45) would keep D185 closer to D112 and

facilitate salt-bridge formation with R211, as we saw in our depolarized model.

The internal salt-bridge network configurations in our models are similar to those observed by Gianti et al. (31), who also used the mHv1cc structure as a template with three different alignments of the three arginine residues on S4 to generate structural ensembles of resting (R), intermediate-resting (IR), and activated states (A). Our unpolarized model resembles the IR-state model, with R205 in contact with D112 and D185 at approximately the same height within the pore. Even the E153–R208 and D174–R211 salt-bridges are observed in both models. When we apply the hyperpolarized potential to the membrane, the arginine residues move down in the pore below F150, resembling the R-state model; R205 is pulled away from D185, leaving the R205–D112 salt-bridge intact.

When comparing the A-state model from Gianti et al. (31) with our fully depolarized configuration, we observed a larger translation of the S4 arginine residues. R205 was pulled up into the extracellular vestibule, forming a stable salt-bridge with D123 at the top of S1. R208 also reached upward in order to form salt-bridges with E119 and E192. This left R211 level with D112 and D185 in the pore. This salt-bridge pattern is similar to the open-state homology model proposed by Chamberlin et al. (30), with R211 passing F150 and the residues they classify as the hydrophobic plug to facilitate interactions with D112 and D185. We did not, however, observe the complete hydrophobic plug that
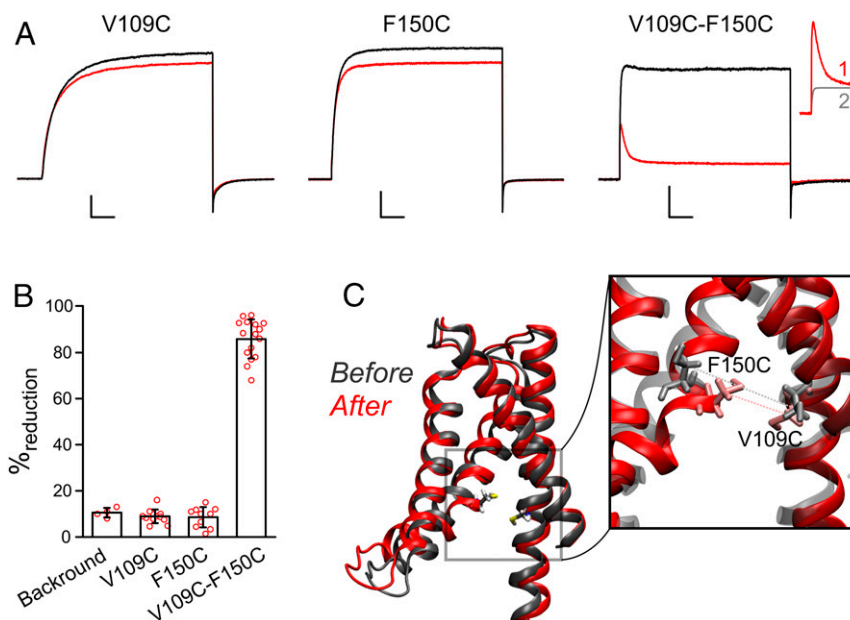
Fig. 4. (*A*) Proton currents from the indicated cysteine mutants (on monomeric Hv1 C107A background) measured in response to depolarization from –40 to +120 mV in the absence (black traces) and presence of 2 μM intracellular Cd^{2+} (red traces). (Horizontal scale bars: 0.1 s; vertical scale bars: 50 pA [V109C], 100 pA [F150C], or 40 pA [V109C–F150C].) *A*, *Right*, *Inset* shows the initial part of the current trace recorded in the presence of Cd^{2+} in more detail (1). The peak indicates that the channel opens before becoming blocked by the metal ion. An alternative situation in which Cd^{2+} binds a closed/nonconducting state would be expected to produce no peak (2). (*B*) Average percentage of reduction of current induced by Cd^{2+}. Data are means ± SDs (values from individual experiments are shown as red circles). (*C*) Hv1 VSD after (red) application of a V109C–F150C S-Cd-S restraint, starting with the open-state model generated during the unrestrained Anton simulation (gray). The distance between the two C_β atoms, to which the restraint force was applied, is shown with dashed lines. The transmembrane helix C_α rmsd of the two structures is ∼1 Å.

they did in the closed state with all three arginine residues sitting below that region.

In agreement with mutagenesis analysis from Randolph et al. (32), R3 in the activated state is in close contact with both D112 and D185. Their homology models for the resting and activated states of Hv1 suggest a larger movement of S4, as much as 14 to 16 Å, although they report a similar effective gating charge of 2.5*e*. However, it is unclear how their results, which are not connected through an actual conformational change induced by a change in applied membrane potential, can be compared to the ones reported here.

On the other side of the spectrum of predicted S4 transmembrane displacements, the crystal structures of the VSD of Ci-VSP captured in the activated and resting states by Li et al. (45) showed a difference in S4 position along the membrane normal of only 5 Å. In their activated state, R3 is in plane with the hydrophobic gasket formed by the conserved F161 (F150 in hHV1). They propose a one-click displacement of the gating charges upon translation and rotation of S4. In our fully depolarized model, all three arginine residues have moved above F150.

Lee et al. (46) used the mHv1cc and Kv1.2 VSD structures as templates for homology models of the Hv1 closed and opened states, respectively, to address the role of D112 in the energetics of Hv1 proton transfer. Their free-energy calculations indicate that the electrostatic barrier to proton transfer posed by the S4 arginines can be overcome via translocation through D112 only in a configuration of the VSD where all of the arginine side chains are in the VSD extracellular crevice. This is in agreement with the overall contrast between our hyperpolarized and fully depolarized configurations. In particular, the requirement of a favorable electrostatic environment to proton transfer is qualitatively consistent with our observation that connected H bond

chain configurations between water molecules and acidic side chains are only found in the fully depolarized state.

The NMR structure of hHv1 in detergent micelles by Bayrhuber et al. (27) is proposed to be in an intermediate state between the resting and fully activated channel. The NMR structure to which we compare was selected from a 100-conformer ensemble having the lowest target function from nuclear Overhauser enhancement-distance restraints. For our resting-state models under both unpolarized and hyperpolarized membrane potentials, the S4 helix is lower by approximately one complete helical turn. A major difference is found in the tilt of the S2 helix. In the NMR structure, all four helices sit perpendicular to the membrane, while in our resting-state structure, the S2 helix is positioned forming a smaller angle with the membrane plane (as seen in *SI Appendix*, Fig. S11).

The difference in the S2 position between our Hv1 models and the NMR structure is most likely caused by the same factors that changed the tilt of S2 during the equilibration of our initial homology model in the membrane environment. In the absence of a phospholipid bilayer, the VSD transmembrane segments tend to be more stable when they assume a parallel configuration that maximizes interhelical interactions. This is also the case in the presence of the phospholipid bilayer when the lengths of all of the transmembrane segments match the thickness of the membrane (47). However, in the Hv1 VSD, S2 is a particularly long helix that would significantly protrude from the membrane plane if it were forced to remain parallel to the other helices. We propose that the major cause of the tilt in S2 seen in our model is driven by the optimization of interhelical interactions and the interactions between the S2 helix and the surrounding phospholipid bilayer.

Concluding Remarks. Our 10-μs-timescale MD simulations of hHv1 VSD embedded in a hydrated lipid bilayer under applied membrane potentials provide putative open- and closed-state models of

the Hv1 channel that are in good agreement with several experimental observables, including the monomeric gating charge, 2GBI binding and mutagenesis, and metal-ion-bridge cross-linking. The models were generated in a way that is independent of any specific assumption on the extent of S4 movement between closed and open states and does not rely on homology and functional similarities between Hv1 and other voltage-sensitive proteins of known structure. They can serve as independent validation of specific structural features observed in previous models, and they can be the basis for further structural refinement using experimental data, including additional cross-links. The models also provide all-atom structures for which explicit modeling of proton transfer can be performed by using quantum chemical calculations. Additionally, they can be used as starting structures, or at least a library of structures, for which computational studies of small-ligand binding can be performed.

Materials and Methods

Model Construction. The initial configuration of the hHv1 monomer resting state was generated by comparative modeling using the mmHv1cc crystal structure (Protein Data Bank ID code 3WKV) as template with the alignment reported by Takeshita et al. (26). The missing loops between the transmembrane segments were constructed by using the Phyre2 web server for homology modeling (48). The S4 segment was truncated at E227, as it has been shown that truncating the coiled-coil segment from the C terminus results in the formation of functional monomeric channels (20, 21). The final hHv1 construct was composed of residues F88 to R230. This protein was inserted into a lipid bilayer consisting of 174 POPC molecules, allowing the putative S0 helix (residues F88 to S97) to be in the phosphate headgroup region of the bilayer and unburying the shortest extracellular loop between S1 and S2. Using CHARMM-GUI (49), the bilayer system was solvated with 10,788 water molecules, and 150 mM NaCl (34 Na$^+$, 38 Cl$^-$) for a total of 58,241 atoms. The initial simulation cell size was 81.5 Å × 81.5 Å × 88.3 Å^3.

Minimization and Equilibration. Initial simulations were performed by using NAMD (Version 2.9) (50). The CHARMM27 (51, 52) and CHARMM36 (53) force fields were used for the protein and lipids, respectively, and the TIP3P model was used for water (54). After 5,000 steps of conjugate energy minimization, the system was run for 100 ps at constant temperature (300 K) and constant volume with all protein atoms constrained, allowing the lipid and water molecules to relax. The system was then equilibrated for 5 ns at constant temperature (300 K) and pressure (1 bar), with the protein-backbone atoms harmonically restrained to their initial positions and then slowly released over an additional 10 ns using a decreasing force constant equal to 50; 25; 10; 5; and 2 kcal·mol^{-1}·Å^{-1}. After the backbone was completely released, we ran an unrestrained simulation for 10 ns.

Microsecond-Timescale Simulation Details. After several nanoseconds of equilibration with NAMD, the system was transferred to Anton, a special-purpose computer for MD simulations of biomolecules, and simulated for 34 μs (55). The CHARMM27 (51, 52) and CHARMM36 (53) force fields were used for the protein and lipids, respectively, and the TIP3P model was used for water (54). An r-RESPA algorithm (56) was employed to integrate the equations of motion with a time step of 6 fs for the long-range nonbonded forces and 2 fs for short-range nonbonded and bonded forces. The k-Gaussian split Ewald method (57) was used for long-range electrostatic interactions. All bond lengths involving hydrogen atoms were constrained using SHAKE (58). The simulations were performed at constant temperature (300 K) and pressure (1 atm), using Nosé–Hoover chains (59) and the Martyna–Tobias–Klein barostat (60). The RESPA algorithm and the temperature and pressure controls were implemented using the multigrator scheme (61).

Gating Charge Estimates. The instantaneous charge displacement with respect to the initial configuration, Δq, was calculated as

$$\Delta q(t) = \sum_i q_i(\phi[\vec{r}_i(t)] - \phi[\vec{r}_i(0)]),$$

where t is time, ϕ is the fractional membrane potential, and $\vec{r}_i$ and q_i are, respectively, the position and partial charge of the ith atom. The sum was taken over all of the atoms constituting the centers of charge of all of the hHv1 monomer basic and acidic side chains according to the CHARMM

force field. Total charge displacement, Q, and per-residue values were computed as

$$Q = \langle \Delta q \rangle_d - \langle \Delta q \rangle_h,$$

where $\langle \Delta q \rangle_d$ and $\langle \Delta q \rangle_h$ are, respectively, the average charge displacement over 40 configurations spanning the last 1.2 μs of the depolarized and hyperpolarized portions of the trajectory.

The membrane potential was calculated by using linearized Poisson–Boltzmann theory, treating all of the system components as linear, isotropic dielectrics under an applied potential difference across the membrane (62–64). For a given configuration along the simulation trajectory, the calculation was performed over a composite system consisting of the atomistic configurations of the protein and lipids in a 70- × 64- × 60-Å^3 region centered on the protein embedded in a continuum, comprised of a semi-infinite planar slab, representing the membrane, between two half-spaces representing the electrolyte solution (64). The continuum-slab thickness was set to be equal to the separation between carbonyl distributions in the atomistic system. The calculations were performed by using the PBEQ module of the CHARMM 32a2 software package (65). The linearized Poisson–Boltzmann equation was solved by finite differences, using the successive overrelaxation method, over a cubic grid of 161 nodes with a grid spacing of 1 Å. A dielectric constant of two was assigned to lipids and protein. The solvent dielectric constant was set to 80, and the salt concentration was set to 150 mM. A molecular surface was used to define the atomistic dielectric boundaries using the Lennard–Jones radii from the CHARMM force field.

The 2GBI Docking. Docking calculations were performed by using a Monte Carlo simulated annealing method implemented in the AutoDock Vina software package (66). Twenty protein configurations were selected from clustered configurations of the four internal residues in hHv1 that represent the binding site near the center of the pore (D112, R211, F150, and S181) from the last ~10 μs of the trajectory under depolarizing potential, in which S4 was in the up position. The clustering analysis was performed by using VMD (67) with an rmsd cutoff of 2.0 Å for nonhydrogen atoms in these four residues. The centroid structure from each cluster was selected as the target for rigid docking of the 2GBI ligand. Twenty docking poses for 2GBI were generated by AutoDock Vina within the search space confined to a cuboid of dimensions 33 × 33 × 24 Å^3 in the intracellular vestibule of the pore. The 400 poses were clustered with a 1.0-Å rmsd cutoff for nonhydrogen atoms of 2GBI.

An identical docking simulation was performed on the closed state by using the ~4-μs trajectory of hHv1 with a hyperpolarizing potential. The binding site for the closed-state clustering was chosen to be the four residues D112, R205, F150, and S181.

Cadmium Cross-Linking. The monomeric version of Hv1 used for the electrophysiological measurements was obtained by replacing the N and C termini of the human channel with the corresponding parts of Ci-VSP as reported (21, 68). Mutations C107A, V109C, and F150C were introduced by using standard mutagenesis approaches as described (21, 36). Complementary DNA constructs in pGEMHE (69) were linearized with SphI restriction enzyme (New England Biolabs) and transcribed by using T7 RNA polymerase (mMessage mMachine, Ambion). A total of 50 to 75 ng of messenger RNA was injected in *Xenopus* oocytes (Ecocyte Bioscience) 2 to 3 d before the electrophysiological measurements. Cells were kept at 18 °C in medium containing 96 mM NaCl, 2 mM KCl, 1.8 mM CaCl$_2$, 1 mM MgCl$_2$, and 10 mM Hepes (pH 7.2), supplemented with 5 mM pyruvate and 100 mg/mL gentamicin.

Patch-clamp measurements were performed in inside-out configurations by using an Axopatch 200B amplifier controlled by pClamp10 software through an Axon Digidata 1440A (Molecular Devices). Pipettes had 1.5- to 3-MΩ access resistance. All measurements were performed at 22 ± 1 °C. Current traces were filtered at 1 kHz, sampled at 5 kHz, and analyzed with Clampfit10.2 (Molecular Devices) and Origin8.1 (OriginLab). Both bath and pipette solutions contained 100 mM 2-(N-morpholino)-ethanesulfonic acid, 30 mM tetraethylammonium (TEA) methanesulfonate, and 5 mM TEA chloride, adjusted to pH 6.0 with TEA hydroxide. The Cd-containing solution was prepared by dissolving CdCl$_2$ in the bath solution to a final concentration of 2 μM. The recording chamber was perfused under gravity with bath solution with or without cadmium by manifold connected to a VC-6 perfusion valve system (Warner Instruments) controlled by the pClamp software by transistor–transistor logic signal.

Data Availability. All necessary data are available in the manuscript and *SI Appendix*. Additional raw data are available upon request.

1. T. E. Decoursey, Voltage-gated proton channels and other proton transfer pathways. *Physiol. Rev.* **83**, 475–579 (2003).
2. Y. Okochi, M. Sasaki, H. Iwasaki, Y. Okamura, Voltage-gated proton channel is expressed on phagosomes. *Biochem. Biophys. Res. Commun.* **382**, 274–279 (2009).
3. I. S. Ramsey, E. Ruchti, J. S. Kaczmarek, D. E. Clapham, Hv1 proton channels are required for high-level NADPH oxidase-dependent superoxide production during the phagocyte respiratory burst. *Proc. Natl. Acad. Sci. U.S.A.* **106**, 7642–7647 (2009).
4. A. El Chemaly et al., VSOP/Hv1 proton channels sustain calcium entry, neutrophil migration, and superoxide production by limiting cell depolarization and acidification. *J. Exp. Med.* **207**, 129–139 (2010).
5. M. Capasso et al., HVCN1 modulates BCR signal strength via regulation of BCR-dependent generation of reactive oxygen species. *Nat. Immunol.* **11**, 265–272 (2010).
6. P. V. Lishko, I. L. Botchkina, A. Fedorenko, Y. Kirichok, Acid extrusion from human spermatozoa is mediated by flagellar voltage-gated proton channel. *Cell* **140**, 327–337 (2010).
7. P. V. Lishko, Y. Kirichok, The role of Hv1 and CatSper channels in sperm activation. *J. Physiol.* **588**, 4667–4672 (2010).
8. D. Iovannisci, B. Illek, H. Fischer, Function of the HVCN1 proton channel in airway epithelia and a naturally occurring mutation, M91T. *J. Gen. Physiol.* **136**, 35–46 (2010).
9. E. Hondares et al., Enhanced activation of an amino-terminally truncated isoform of the voltage-gated proton channel HVCN1 enriched in malignant B cells. *Proc. Natl. Acad. Sci. U.S.A.* **111**, 18078–18083 (2014).
10. Y. Wang et al., Specific expression of the human voltage-gated proton channel Hv1 in highly metastatic breast cancer cells, promotes tumor progression and metastasis. *Biochem. Biophys. Res. Commun.* **412**, 353–359 (2011).
11. Y. Wang, S. J. Li, X. Wu, Y. Che, Q. Li, Clinicopathological and biological significance of human voltage-gated proton channel Hv1 protein overexpression in breast cancer. *J. Biol. Chem.* **287**, 13877–13888 (2012).
12. Y. Wang, X. Wu, Q. Li, S. Zhang, S. J. Li, Human voltage-gated proton channel Hv1: A new potential biomarker for diagnosis and prognosis of colorectal cancer. *PLoS One* **8**, e70550 (2013).
13. L.-J. Wu et al., The voltage-gated proton channel Hv1 enhances brain damage from ischemic stroke. *Nat. Neurosci.* **15**, 565–573 (2012).
14. T. Kawai et al., Unconventional role of voltage-gated proton channels (VSOP/Hv1) in regulation of microglial ROS production. *J. Neurochem.* **142**, 686–699 (2017).
15. T. Seredenina, N. Demaurex, K. H. Krause, Voltage-gated proton channels as novel drug targets: From NADPH oxidase regulation to sperm biology. *Antioxid. Redox Signal.* **23**, 490–513 (2015).
16. F. J. Morera et al., Voltage-dependent BK and Hv1 channels expressed in non-excitable tissues: New therapeutics opportunities as targets in human diseases. *Pharmacol. Res.* **101**, 56–64 (2015).
17. J. A. Freites, D. J. Tobias, Voltage sensing in membranes: From macroscopic currents to molecular motions. *J. Membr. Biol.* **248**, 419–430 (2015).
18. I. S. Ramsey, M. M. Moran, J. A. Chong, D. E. Clapham, A voltage-gated proton-selective channel lacking the pore domain. *Nature* **440**, 1213–1216 (2006).
19. M. Sasaki, M. Takagi, Y. Okamura, A voltage sensor-domain protein is a voltage-gated proton channel. *Science* **312**, 589–592 (2006).
20. H. P. Koch et al., Multimeric nature of voltage-gated proton channels. *Proc. Natl. Acad. Sci. U.S.A.* **105**, 9111–9116 (2008).
21. F. Tombola, M. H. Ulbrich, E. Y. Isacoff, The voltage-gated proton channel Hv1 has two pores, each controlled by one voltage sensor. *Neuron* **58**, 546–556 (2008).
22. S. A. Pless, J. D. Galpin, A. P. Niciforovic, C. A. Ahern, Contributions of counter-charge in a potassium channel voltage-sensor domain. *Nat. Chem. Biol.* **7**, 617–623 (2011).
23. J. A. Freites, E. V. Schow, S. H. White, D. J. Tobias, Microscopic origin of gating current fluctuations in a potassium channel voltage sensor. *Biophys. J.* **102**, L44–L46 (2012).
24. M. O. Jensen et al., Mechanism of voltage gating in potassium channels. *Science* **336**, 229–233 (2012).
25. Q. Li et al., Structural mechanism of voltage-dependent gating in an isolated voltage-sensing domain. *Nat. Struct. Mol. Biol.* **21**, 244–252 (2014).
26. K. Takeshita et al., X-ray crystal structure of voltage-gated proton channel. *Nat. Struct. Mol. Biol.* **21**, 352–357 (2014).
27. M. Bayrhuber et al., Nuclear magnetic resonance solution structure and functional behavior of the human proton channel. *Biochemistry* **58**, 4017–4027 (2019).
28. M. L. Wood et al., Water wires in atomistic models of the Hv1 proton channel. *Biochim. Biophys. Acta* **1818**, 286–293 (2012).
29. K. Kulleperuma et al., Construction and validation of a homology model of the human voltage-gated proton channel hHV1. *J. Gen. Physiol.* **141**, 445–465 (2013).
30. A. Chamberlin et al., Hydrophobic plug functions as a gate in voltage-gated proton channels. *Proc. Natl. Acad. Sci. U.S.A.* **111**, E273–E282 (2014).
31. E. Gianti, L. Delemotte, M. L. Klein, V. Carnevale, On the role of water density fluctuations in the inhibition of a proton channel. *Proc. Natl. Acad. Sci. U.S.A.* **113**, E8359–E8368 (2016).
32. A. L. Randolph, Y. Mokrab, A. L. Bennett, M. S. P. Sansom, I. S. Ramsey, Proton currents constrain structural models of voltage sensor activation. *eLife* **5**, e18017 (2016).
33. V. De La Rosa, I. S. Ramsey, Gating currents in the Hv1 proton channel. *Biophys. J.* **114**, 2844–2854 (2018).
34. Y. Fujiwara et al., The cytoplasmic coiled-coil mediates cooperative gating temperature sensitivity in the voltage-gated H(+) channel Hv1. *Nat. Commun.* **3**, 816 (2012).
35. C. Gonzalez, H. P. Koch, B. M. Drum, H. P. Larsson, Strong cooperativity between subunits in voltage-gated proton channels. *Nat. Struct. Mol. Biol.* **17**, 51–56 (2010).
36. L. Hong, M. M. Pathak, I. H. Kim, D. Ta, F. Tombola, Voltage-sensing domain of voltage-gated proton channel Hv1 shares mechanism of block with pore domains. *Neuron* **77**, 274–287 (2013).
37. L. Hong, I. H. Kim, F. Tombola, Molecular determinants of Hv1 proton channel inhibition by guanidine derivatives. *Proc. Natl. Acad. Sci. U.S.A.* **111**, 9971–9976 (2014).
38. P. G. DeCaen, V. Yarov-Yarovoy, E. M. Sharp, T. Scheuer, W. A. Catterall, Sequential formation of ion pairs during activation of a sodium channel voltage sensor. *Proc. Natl. Acad. Sci. U.S.A.* **106**, 22498–22503 (2009).
39. P. G. DeCaen, V. Yarov-Yarovoy, Y. Zhao, T. Scheuer, W. A. Catterall, Disulfide locking a sodium channel voltage sensor reveals ion pair formation during activation. *Proc. Natl. Acad. Sci. U.S.A.* **105**, 15142–15147 (2008).
40. V. Yarov-Yarovoy et al., Structural basis for gating charge movement in the voltage sensor of a sodium channel. *Proc. Natl. Acad. Sci. U.S.A.* **109**, E93–E102 (2012).
41. U. Henrion et al., Tracking a complete voltage-sensor cycle with metal-ion bridges. *Proc. Natl. Acad. Sci. U.S.A.* **109**, 8552–8557 (2012).
42. D. Morgan et al., Peregrination of the selectivity filter delineates the pore of the human voltage-gated proton channel hHV1. *J. Gen. Physiol.* **142**, 625–640 (2013).
43. R. Banh et al., Hydrophobic gasket mutation produces gating pore currents in closed human voltage-gated proton channels. *Proc. Natl. Acad. Sci. U.S.A.* **116**, 18951–18961 (2019).
44. F. Tombola, M. H. Ulbrich, S. C. Kohout, E. Y. Isacoff, The opening of the two pores of the Hv1 voltage-gated proton channel is tuned by cooperativity. *Nat. Struct. Mol. Biol.* **17**, 44–50 (2010).
45. Q. Li et al., Resting state of the human proton channel dimer in a lipid bilayer. *Proc. Natl. Acad. Sci. U.S.A.* **112**, E5926–E5935 (2015).
46. M. Lee, C. Bai, M. Feliks, R. Alhadeff, A. Warshel, On the control of the proton current in the voltage-gated proton channel Hv1. *Proc. Natl. Acad. Sci. U.S.A.* **115**, 10321–10326 (2018).
47. A. Y. Tronin et al., Voltage-dependent profile structures of a Kv-channel via time-resolved neutron interferometry. *Biophys. J.* **117**, 751–766 (2019).
48. L. A. Kelley, S. Mezulis, C. M. Yates, M. N. Wass, M. J. E. Sternberg, The Phyre2 web portal for protein modeling, prediction and analysis. *Nat. Protoc.* **10**, 845–858 (2015).
49. S. Jo, T. Kim, V. G. Iyer, W. Im, CHARMM-GUI: A web-based graphical user interface for CHARMM. *J. Comput. Chem.* **29**, 1859–1865 (2008).
50. J. C. Phillips et al., Scalable molecular dynamics with NAMD. *J. Comput. Chem.* **26**, 1781–1802 (2005).
51. A. D. MacKerell et al., All-atom empirical potential for molecular modeling and dynamics studies of proteins. *J. Phys. Chem. B* **102**, 3586–3616 (1998).
52. A. D. Mackerell, Jr, M. Feig, C. L. Brooks, 3rd, Extending the treatment of backbone energetics in protein force fields: Limitations of gas-phase quantum mechanics in reproducing protein conformational distributions in molecular dynamics simulations. *J. Comput. Chem.* **25**, 1400–1415 (2004).
53. J. B. Klauda et al., Update of the CHARMM all-atom additive force field for lipids: Validation on six lipid types. *J. Phys. Chem. B* **114**, 7830–7843 (2010).
54. W. L. Jorgensen, J. Chandrasekhar, J. D. Madura, R. W. Impey, M. L. Klein, Comparison of simple potential functions for simulating liquid water. *J. Chem. Phys.* **79**, 926–935 (1983).
55. D. E. Shaw et al., Anton, a special-purpose machine for molecular dynamics simulation. *Commun. ACM* **51**, 91–97 (2008).
56. M. Tuckerman, B. J. Berne, G. J. Martyna, Reversible multiple time scale molecular dynamics. *J. Chem. Phys.* **97**, 1990–2001 (1992).
57. Y. Shan, J. L. Klepeis, M. P. Eastwood, R. O. Dror, D. E. Shaw, Gaussian split Ewald: A fast Ewald mesh method for molecular simulation. *J. Chem. Phys.* **122**, 54101 (2005).
58. J.-P. Ryckaert, G. Ciccotti, H. J. C. Berendsen, Numerical integration of the Cartesian equations of motion of a system with constraints: Molecular dynamics of n-alkanes. *J. Comput. Phys.* **23**, 327–341 (1977).
59. G. J. Martyna, M. L. Klein, M. Tuckerman, Nosé–Hoover chains: The canonical ensemble via continuous dynamics. *J. Chem. Phys.* **97**, 2635 (1992).

BIOPHYSICS AND
COMPUTATIONAL BIOLOGY

60. G. J. Martyna, D. J. Tobias, M. L. Klein, Constant pressure molecular dynamics algorithms. *J. Chem. Phys.* **101**, 4177 (1994).

61. R. A. Lippert *et al.*, Accurate and efficient integration for molecular dynamics simulations at constant temperature and pressure. *J. Chem. Phys.* **139**, 164106 (2013).

62. B. Roux, Influence of the membrane potential on the free energy of an intrinsic protein. *Biophys. J.* **73**, 2980–2989 (1997).

63. M. Grabe, H. Lecar, Y. N. Jan, L. Y. Jan, A quantitative assessment of models for voltage-dependent gating of ion channels. *Proc. Natl. Acad. Sci. U.S.A.* **101**, 17640–17645 (2004).

64. B. Roux, The membrane potential and its representation by a constant electric field in computer simulations. *Biophys. J.* **95**, 4205–4216 (2008).

65. B. R. Brooks *et al.*, CHARMM: The biomolecular simulation program. *J. Comput. Chem.* **30**, 1545–1614 (2009).

66. O. Trott, A. J. Olson, AutoDock Vina: Improving the speed and accuracy of docking with a new scoring function, efficient optimization, and multithreading. *J. Comput. Chem.* **31**, 455–461 (2010).

67. W. Humphrey, A. Dalke, K. Schulten, VMD: Visual molecular dynamics. *J. Mol. Graph.* **14**, 33–38 (1996).

68. L. Hong, V. Singh, H. Wulff, F. Tombola, Interrogation of the intersubunit interface of the open Hv1 proton channel with a probe of allosteric coupling. *Sci. Rep.* **5**, 14077 (2015).

69. E. R. Liman, J. Tytgat, P. Hess, Subunit stoichiometry of a mammalian K+ channel determined by construction of multimeric cDNAs. *Neuron* **9**, 861–871 (1992).